Received: 21 February 2024 | Revised: 15 May 2024 | Accepted: 1 October 2024 | Published online: 8 October 2024

RESEARCH ARTICLE

Journal of Optics and Photonics Research
2026, Vol. 3(2) 109–121
DOI: 10.47852/bonviewJOPR42022660

BON VIEW PUBLISHING

Structural Analysis Technique and Its Validation for Large Range Mirror Refocusing System for Spaceborne Deployable Telescopes

Yesh Pal[1,*], Rahul Dev[1], Naimesh R. Patel[1], Neeraj Mathur[1], Shaunak R. Joshi[1] and Harshraj Dod[2]

[1]*Space Applications Centre, Indian Space Research Organization, India*

[2]*Lalbhai Dalpatbhai College of Engineering, India*

Abstract: Large aperture deployable telescopes with numerous onboard instruments are popular in the space industry for astronomy. Scientific data in various wavelength bands, from 0.6 μ to 28 μ, are provided by these instruments and are crucial for deep space exploration. The deployment mechanisms handle the alignment and functionality at the telescope level only. At instrument level, there is always a need for a refocusing system which can cater individual need of instrument for focusing independent to other instruments nearby. In this paper, we present a structural analysis technique for such a type of large range mirror refocusing mechanism, similar to the near-infrared spectrograph payload of the James Webb Space Telescope. The method relies on geometric non-linearity for large deflection, in which the structure's stiffness matrix changes as a function of loading. We have designed, analyzed structurally, and tested a 4 mm range slider crank-based compliant mechanism. The outcomes of linear and non-linear static analysis, computed numerically, have been compared. There are noticeable significant variations in one direction between the two analyses' results. The results are validated using appropriately designed and realized test setups, like measurements of displacement, changes in focus and image position of the optical system.

Keywords: mirror, telescope, displacement, refocusing, stiffness, direction

1. Introduction

For deep space exploration, the demand for high-resolution scientific data in different wavelength bands is increasing in the space industry. For this, a single electro-optical (EO) payload must contain multiple instruments. A large aperture telescope is necessary for high resolution. Furthermore, additional envelope is needed to fit multiple instruments within a single telescope. Monolithic large aperture telescopes with maximum diameter of 3.5 meters have been flown in numerous space missions [1]. Beyond this size, manufacturing of monolithic mirrors is difficult. To overcome this, space agencies are opting for deployable telescopes with segmented mirrors, which can be deployed in space [2]. The deployment can be done through appropriate mechanisms.

These mechanisms will only take care of alignment and performance at telescope level. At instrument level, there is always a need of focusing [3] due to gravity release and thermo-elastic deformations [4–6]. These are integrated ahead of the image plane in the optical path. Therefore, a wide range with low hysteresis and good repeatability is needed for these mechanisms. To cater this, a compliant mechanism [7–12] with flexural hinge joints is generally used instead of an ideal hinge [13–17].

These mechanisms pose significant advantages over rigid mechanisms in terms of precise motion without backlash, light in weight, no wear and tear, etc. They facilitate mobility by means of the elastic deformation of flexible components, like flexure hinges [16–19].

Mondello et al. [20] presented one such type of compliant mechanism used in the near-infrared spectrograph payload of the James Webb Space Telescope project, which covers the 0.6 μ to 5 μ wavelength range. It is based on the crank-lever concept. The slider movement of 6 mm is achieved by three flexural blades and an eccentric shaft of 3 mm eccentricity. The shaft is connected to the slider through a lever with a flexural hinge joint. The main function of this mechanism was to move a set of two plane mirrors in a common refocusing direction.

In this paper, we have examined and implemented structural analysis technique for a large deflection compliant mechanism. For the case study, a mechanism similar to Mondello et al. [20] with a 4 mm stroke has been designed, structurally analyzed, realized, and tested. The technique is a simulation of geometric non-linearity due to large deformations of flexure hinges where stiffness is varying with respect to loading at each step.

Bahari et al. [21] presented simulation and testing on the non-linearity behavior of a slender cantilever beam. The results of linear and non-linear static analysis are compared with test results and successfully judge the geometric non-linear deflection behavior of a beam.

Geometric non-linearity problems can be solved using various techniques [22–25]. The Newton Raphson [22] method is the most

***Corresponding author:** Yesh Pal, Space Applications Centre, Indian Space Research Organization, India. Email: yeshpal@sac.isro.gov.in

popular among them. This method of solving problems is incremental iteratively, updating the stiffness matrix at various time or load steps [22, 23]. Finite element (FE) software has been used for the simulation of large deformations due to geometric non-linearity based on Newton Raphson. Initially, mechanism was designed and realized with linear static analysis. Testing revealed that there was mismatch between FE and test results in one direction. Subsequently, a non-linear static analysis technique was discovered and has produced results with test data that are nearly accurate. The test results are compared with the outcomes of both analyses.

Subsequent sections in this paper are organized as follows. Section 2 briefly introduces the case that is being analyzed. The structural analysis method for simulating large deflections is explained in Section 3. Section 4 presents the results of the numerical analysis. Section 5 demonstrates the testing and validation part, where improvement in image quality is demonstrated with the refocusing mechanism. Finally, Section 6 concludes this paper by summarizing finding from numerical and experimental results.

1.1. Generic use of refocusing mechanism in EO deployable telescopes

The mechanism is required to be placed before the image plane in the optical path of a spaceborne EO ritchey–chrétien (RC) telescope as depicted in Figure 1(a). A set of two flat mirrors (*M*1 and *M*2) mounted in a pentaprism arrangement shall be moved by 4 mm along a common axis. The movement of 4 mm results in a change of focus of 5.6 mm by optical system. Figure 1(b) and (c) shows simulated image of United States Air Force (USAF) 1951 bar target through optical systems at defocused and focused condition respectively. Considering the depth of focus of the system, the necessary resolution in such cases is less than 20 microns.

2. Case Study

A mechanism has been designed similar to Mondello et al. [20]. A 4 mm movement of top plate is achieved by 180-degree rotation of eccentric shaft with eccentricity of 2 mm. Two mirrors (*M*1 and *M*2) are mounted on top plate in pentaprism configuration. The top plate is connected to base plate in parallelogram configuration using three flexural blades. These blades serve two purposes, first it allows the movement of slider and secondly it provides adequate stiffness to sustain launch loads. Additionally, these blades have flexure hinges which allow mobility by elastic deformation. Figure 2(a) and (b) depicts different computer-aided design (CAD) views of assembly along with name of parts. Since it is allowing large deformation, stiffness of these blades is different at each step from 0 to 4 mm movement. So, simulation of this behavior is crucial for ensuring perfect linear movement of top plate by minimizing other directions movement and tilts. Reducing movement in other

Figure 1

(a) Generic location of refocusing system in optical path of RC telescope, simulated image of USAF 1951 bar target through optical system, at (b) 5.6 mm defocused, (c) focused

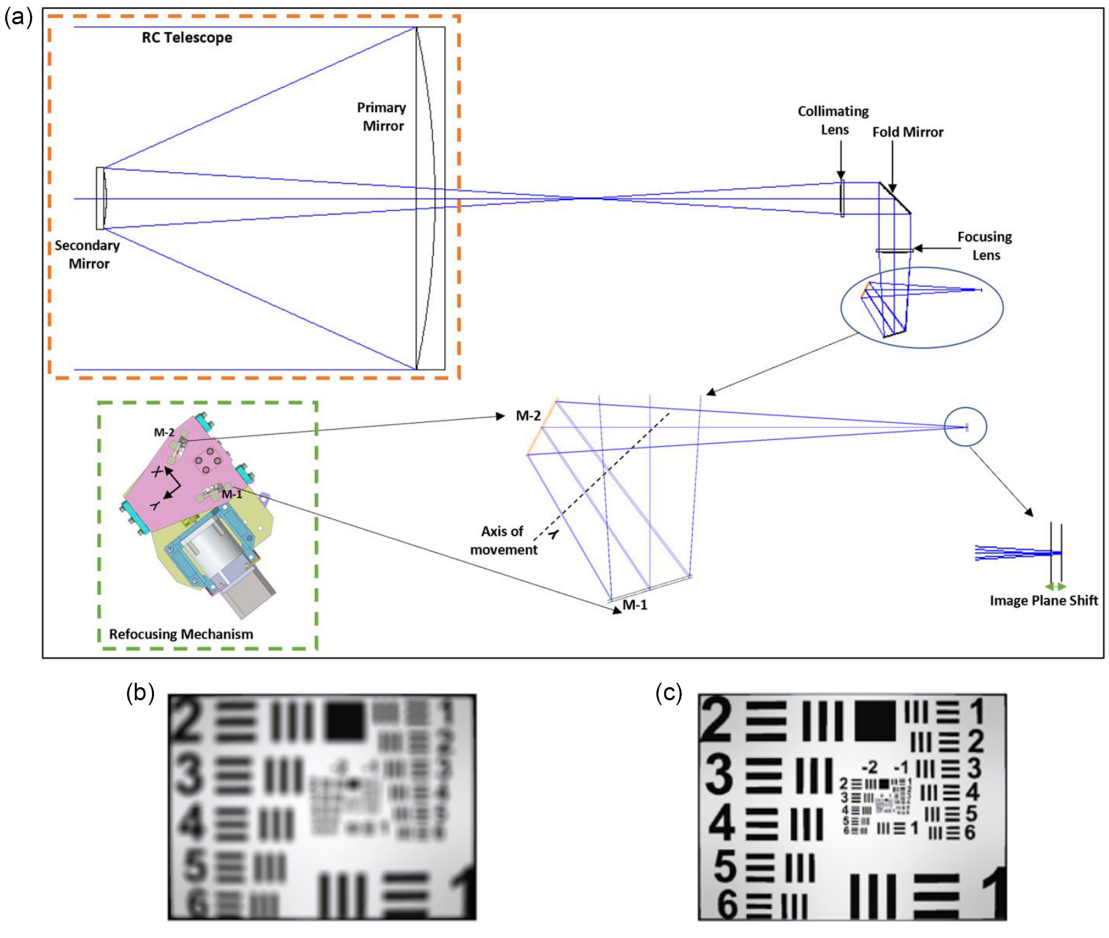

Figure 2

CAD view of assembly (a) orientation of coordinate system w.r.t. mirrors and (b) isometric view showing major parts of mechanism

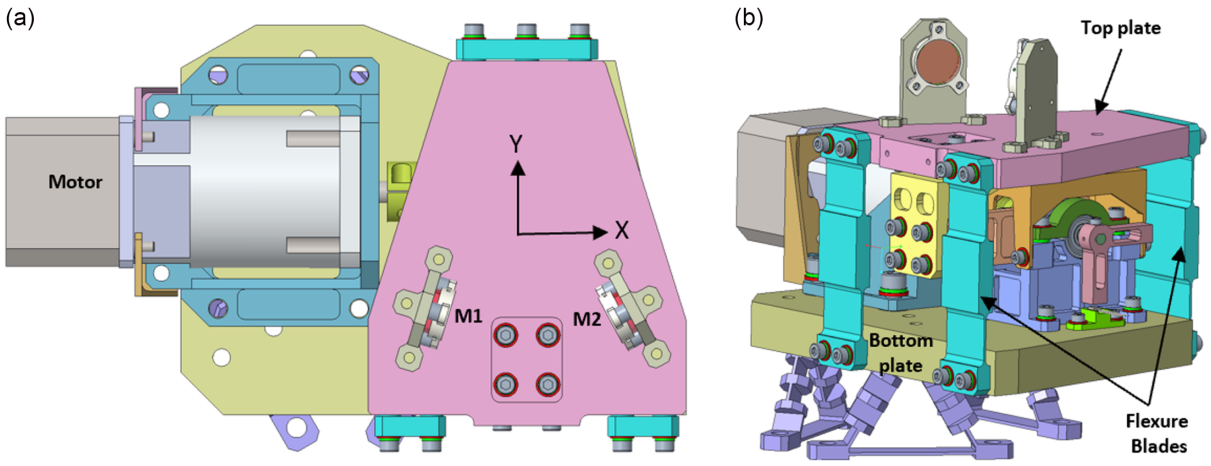

directions will aid in defining tolerances for mirror clear aperture without optical ray vignetting. When the mechanism moves, tilts in both mirrors may cause the system's field of view to be limited, which will reduce the instrument's ability to cover full defined swaths. The designed assembly has an envelope measuring 200 × 125 × 150(H) mm and a total mass of 1.8 kg. Refer Figure 3(a) for different links and joints of slider crank mechanism.

3. Structural Analysis Technique

The design of mechanism is based on slider crank-lever concept. The crank rotation is 180 degree which results in 4 mm of top plate movement. For allowing 4 mm movement, the flexural blades must bend at least by 4 mm which results in large deflection. Due to this, at each step movement, the stiffness of these blades is different. This is resulted due to geometric non-linearity of blades.

In linear finite element analysis (FEA), the equilibrium equation is:

$$F = K * u \tag{1}$$

Where K is stiffness matrix, u is displacement, and F is load vector. The stiffness matrix is constant throughout the process, and it does not depend on displacements and load [22, 23].

In non-linear FEA, stiffness matrix is a function of displacement and load vector.

$$K(u) = F(u) * u^{-1} \tag{2}$$

Here, $K(u)$ is stiffness matrix, u is displacement, and $F(u)$ is load vector which is function of crank displacement computed in Section 3.1. The following equations are widely used Newton Raphson incremental iterative solution method where basic

Figure 3

(a) Different links of mechanism w.r.t. coordinate system and (b) schematic showing crank rotation

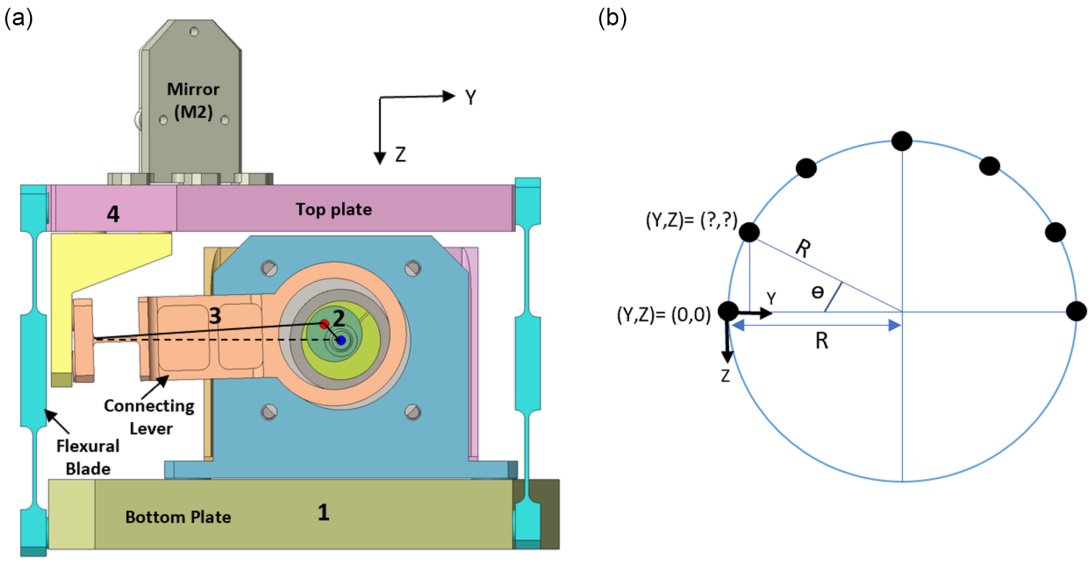

assumption is solution for time t is known and solution for time $t+\Delta t$ is required [22–24].

$$\left({}^{t+\Delta t}K^{(i-1)}\right) * \Delta U^{(i)} = {}^{t+\Delta t}R - {}^{t+\Delta t}F^{(i-1)} \tag{3}$$

where ${}^{t+\Delta t}K^{(i-1)}$ is the current tangent stiffness matrix,

$${}^{t+\Delta t}K^{(i-1)} = \left[\frac{\partial F}{\partial U}\right]\Big|_{{}^{t+\Delta t}U^{(i-1)}} \tag{4}$$

And improved displacement solution is:

$${}^{t+\Delta t}U^{(i)} = {}^{t+\Delta t}U^{(i-1)} + \Delta U^{(i)} \tag{5}$$

With initial conditions for $i=1$,

$${}^{t+\Delta t}U^{(0)} = {}^{t}U\,; \quad {}^{t+\Delta t}F^{(0)} = {}^{t}F\,; \quad {}^{t+\Delta t}K^{(0)} = {}^{t}K\,; \tag{6}$$

where Δt is time or load steps, i is number of iterations varying from 1,2,3 …, n, ${}^{t}K$ is tangent stiffness matrix at time t, ${}^{t}U$ is displacement at time t, ${}^{t}F$ is nodal point force corresponding to element stresses at time t, ${}^{t+\Delta t}R$ is externally applied nodal point force. These iterations continued until appropriate convergence criteria are satisfied.

3.1. Computation of crank displacement

Crank displacement has been computed for defining input load as boundary condition for both linear and non-linear static analysis. The displacement is computed analytically using Equations (7) and (8) as well as from mechanism simulation in FE software for validation. Figure 3(a) and (b) depicts different links of mechanism and schematic of crank rotation respectively.

Table 1 shows type of motion of different links.

Table 1
Different links and their motion

Links	Part name/Link	Type of motion
1	Bottom Plate	Fixed
2	Crank	Rotary
3	Connecting Lever	Linear & Rotary
4	Top Plate	Linear Translation

Value of Y & Z can be computed using below equations.

$$Y = R * (1 - \cos\theta) \tag{7}$$

$$Z = R * \sin\theta \tag{8}$$

where R is eccentricity which is 2 mm and θ is crank rotation ranging from 0 to 180 degrees.

For crank rotation of 30-degree step, the computed values of Y and Z both analytically and numerically are tabled below with comparison. Figure 4(a) and (b) depicts graphs of tabled values with error at each step. The maximum error is 9 μ at 90-degree step for both Y and Z displacements.

3.2. Boundary condition for structural analysis

Three bipods have their bottom lugs fixed in all three directions, as shown in Figure 5(a) by the black horizontal line. For linear static analysis, numerically computed displacements of 0 to 4 mm which is in steps of 30 degree applied at green node marked on connecting lever as shown in zoomed Figure 5(a). This step was chosen in light of the findings of the experiment as well as FE analysis at both coarser and finer steps. For non-linear static analysis, numerically computed displacement in Table 2 along Y and Z direction is applied at both green and blue nodes, respectively. Displacements are applied at these two distinct nodes due to FE software limitation in non-linear static analysis. Both of these nodes are free to move in the Y and Z directions during motion from 0 to 180 degrees or vice versa. Three locations on the top plate ($L1$, $L2$, and $L3$) have been designated for recording displacement in each of the three directions, as depicted in Figure 5(b).

4. FE Results

Both the linear and non-linear static analysis deformation contours are displayed in Figures 6 and 7. In Figure 6(a)–(d), deformation along Y is displayed for both linear and non-linear static analyses. For non-linear analysis, deformation contour at 30-degree step and 90-degree step is also shown in Figure 6(b) and (d). Figure 7(a) and (b) depicts Z direction deformation contour. The computed results are incorporated in Tables 3 and 4. Along X and Y directions, the results of displacement are almost similar for both linear as well as non-linear static analysis.

Figure 4
(a) Graph of crank displacement along Y vs rotation and (b) graph of crank displacement along Z vs rotation

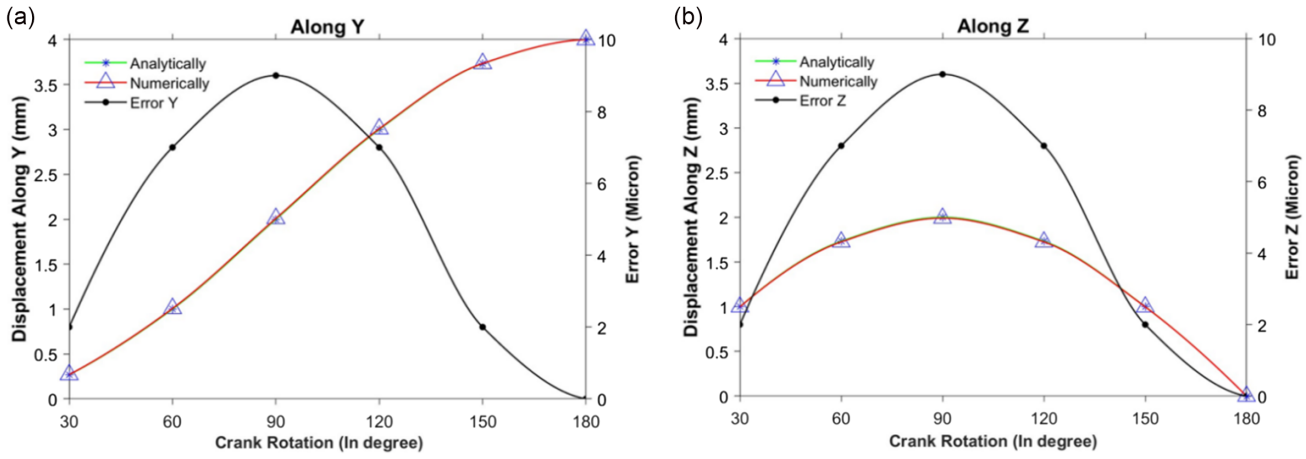

Figure 5
(a) Boundary condition and (b) location of three points/nodes for recording displacement

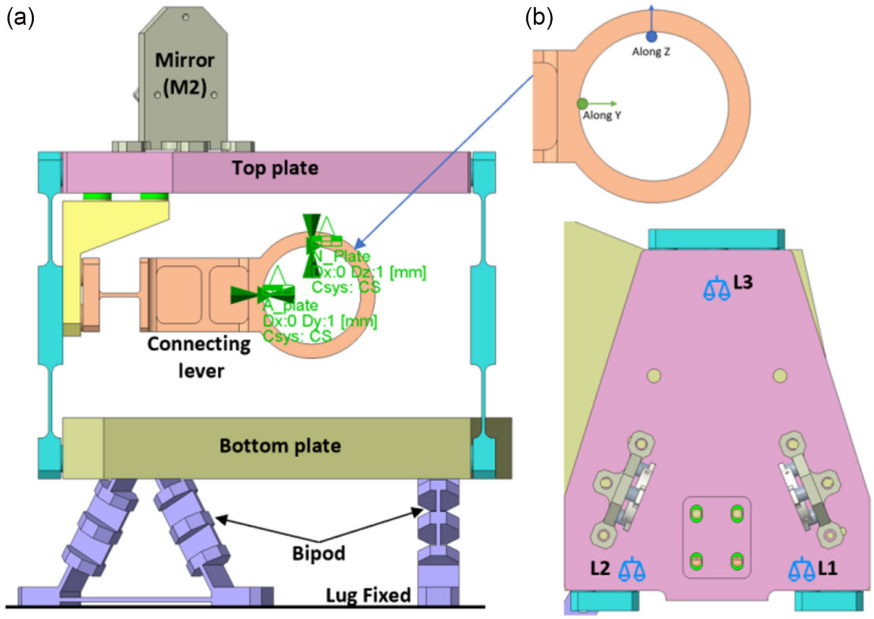

Table 2
Computation of crank displacement

Crank rotation (in degree)	Along Y		Along Z	
	Analytically	Numerically (FE)	Analytically	Numerically (FE)
30	0.268	0.270	1.000	0.998
60	1.000	1.007	1.732	1.725
90	2.000	2.009	2.000	1.991
120	3.000	3.007	1.732	1.725
150	3.732	3.734	1.000	0.998
180	4.000	4.000	0.000	0.000

For the maximum range, the error is less than 1% in the *Y* direction. There is a significant difference between linear and non-linear analysis results along the *Z* direction. From 0 to 180-degree step, the error keeps getting bigger. Figure 8(a) and (b) depicts displacement graphs for linear and non-linear static analysis with error.

4.1. Opto-mechanical analysis for temperature load

An opto-mechanical analysis has been performed for operating temperature loads of 20 ± 5 °C which will be controlled by thermal systems. The alignment stability, mainly tilt numbers, has been computed for both the mirrors. Table 5 shows the computed numbers of tilts in both mirrors with goal.

5. Validation

To validate the design, mechanism is realized as shown in Figure 9. Parallelism of 50 microns between top and bottom plate is ensured during actual assembly of mechanism. Materials used for different parts are mentioned in Table 6. A geared stepper motor is utilized to drive the crank. To power and control the motor, suitable commercial electronics have been utilized.

5.1. Mechanical test setup for displacement validation

A mechanical test setup has been designed and realized to measure the displacement of the top plate along the *Y* and *Z* directions. Displacement along the *Y* direction is measured using a single linear variable differential transformer (LVDT) probe with a 5 mm range and a 0.1-micron resolution. To measure displacement along *Z* direction, three capacitive probes [26] with sub-nanometer resolution and a range of ±250 μ are positioned at *L*1–*L*3 locations. Tilts of the upper plate can also be calculated using reading of these three probes. Three invar-made posts hold these probes in place. Because of its low thermal expansion/contraction, the Invar material has been selected to minimize the impact of temperature variation during measurements. The controller powers the geared stepper motor. The designed and realized mechanical test setups are shown in Figure 10(a) and (b), respectively.

5.2. Optical test setup for validation of refocusing and image position

Using readily available commercial optics, an optical setup has been designed and realized to validate and demonstrate refocusing and inplane movement of image, as shown in Figure 11(a) and (b). A spherical lens of effective focal length 200 mm is used for focusing light on detector plane. Light is being focused by this lens on detector through *M*1 and *M*2 flat mirrors mounted on top plate of mechanism. Table 7 lists specifications of various optical elements.

Furthermore, optical design simulation has been performed to determine the focus shift caused by the movement of these flat mirrors. A 5.6 mm shift in focus is produced by 4 mm movement of the top plate holding two flat mirrors. With an 8 mm beam diameter, system *F*# is 25. The optical design is shown in

Figure 6
Displacement contour along (a) *Y* direction of linear static analysis at 180-degree step, (b) *Y* at 30-degree step of non-linear static analysis, (c) *Y* at 90-degree step of non-linear static analysis, and (d) *Y* at 180-degree step of non-linear static analysis

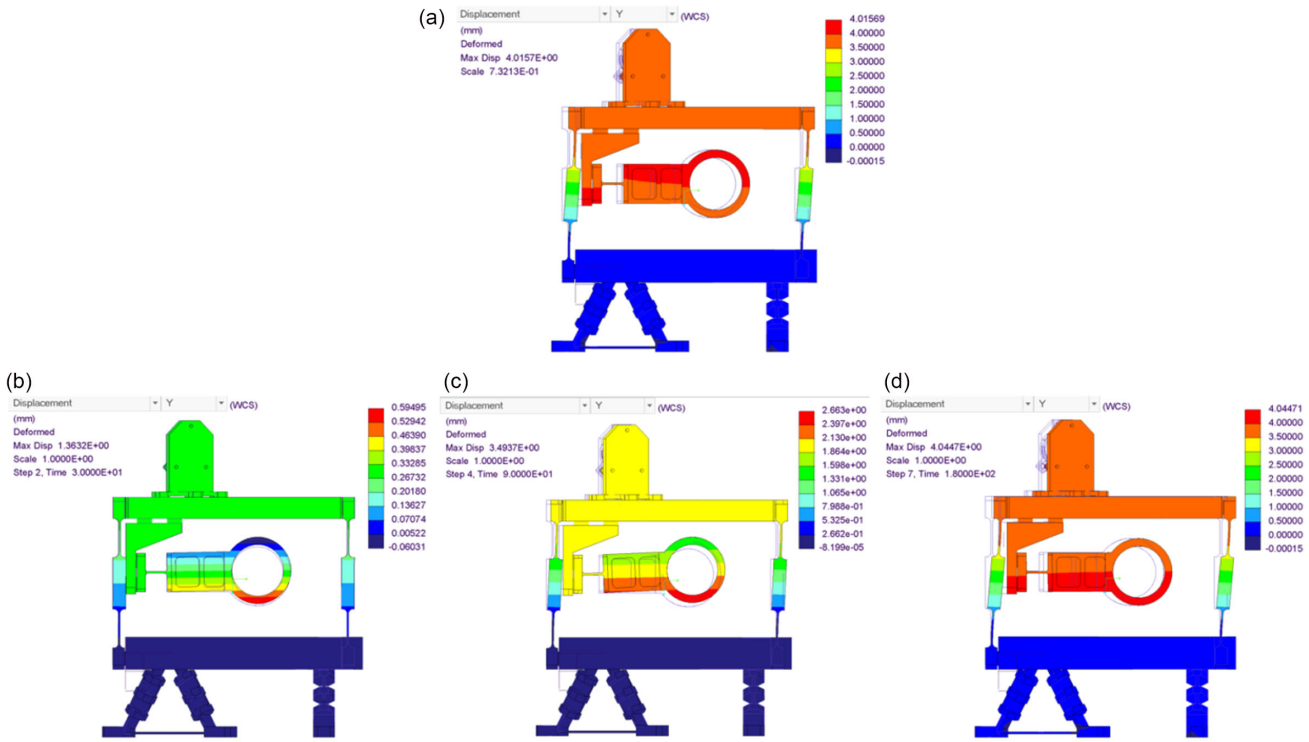

Figure 7
Displacement contour along (a) *Z* direction of linear static analysis at 180-degree step and (b) *Z* at 180-degree step of non-linear static analysis

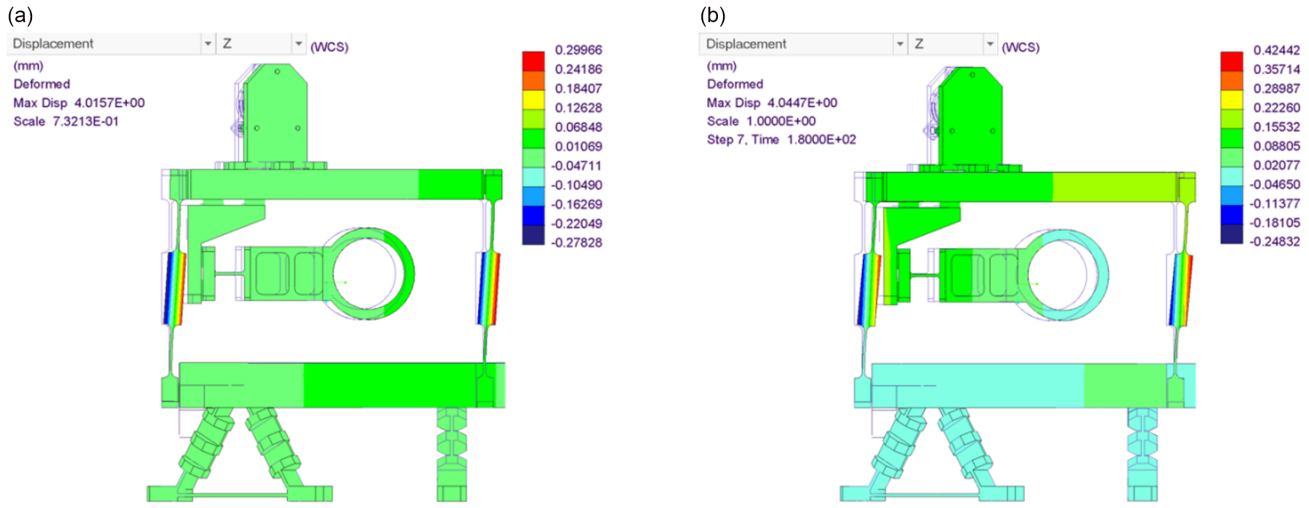

Figure 12(a) and (b) in focused and defocused conditions, respectively. The airy disk diagram with point spread function (PSF) plot at focused and at defocused condition is shown in Figure 12(c)–(f).

5.3. Test results of displacement

The LVDT records displacement in the *Y* direction at the top plate location between *L*1 and *L*2. Three capacitive probes recorded displacement along *Z* directions at *L*1 to *L*3. Table 8 comprises of these results at different rotations. Nearly identical displacements exist along *Z* direction for the locations of *L*1 and *L*2. There is a significant difference between displacement from *L*1 and *L*2 to *L*3 location. This variation causes the top plate to tilt about *X* direction. For a distance of 82.5 mm between these locations, the computed tilt value about *X* direction is 77.5 arcsec. This will have impact on image

Table 3
Computed displacements by linear static analysis at identified locations in all three directions at different angles

Type of analysis	Crank rotation (In degree)	*L*1 displacement (mm)			*L*2 displacement (mm)			*L*3 displacement (mm)		
		X	Y	Z	X	Y	Z	X	Y	Z
Linear Static	30	−0.001	0.263	−0.002	0.000	0.263	−0.001	−0.001	0.264	−0.001
	60	0.000	0.991	−0.004	0.000	0.991	−0.003	0.001	0.992	0.000
	90	0.001	1.983	−0.006	0.002	1.984	−0.004	0.003	1.985	0.004
	120	0.003	2.974	−0.008	0.004	2.976	−0.006	0.007	2.977	0.008
	150	0.005	3.698	−0.008	0.006	3.701	−0.006	0.010	3.702	0.012
	180	0.006	3.966	−0.007	0.007	3.969	−0.006	0.013	3.970	0.015

Table 4
Computed displacements by non-linear static analysis at identified locations in all three directions at different angles

Type of analysis	Crank rotation (In degree)	*L*1 displacement (mm)			*L*2 displacement (mm)			*L*3 displacement (mm)		
		X	Y	Z	X	Y	Z	X	Y	Z
Non-Linear Static	30	0.000	0.271	−0.001	0.000	0.271	0.000	0.000	0.271	0.000
	60	0.000	1.014	0.006	0.000	1.014	0.008	0.001	1.015	0.015
	90	0.001	2.014	0.034	0.002	2.015	0.036	0.003	2.016	0.045
	120	0.003	2.998	0.081	0.003	3.000	0.084	0.006	3.001	0.097
	150	0.004	3.706	0.128	0.005	3.709	0.130	0.010	3.710	0.147
	180	0.006	3.965	0.149	0.006	3.968	0.151	0.001	3.969	0.170

Figure 8
(a) Graph of *Z* direction displacement at *L*3 from FE and (b) graph of *Y* direction displacement at *L*3 from FE

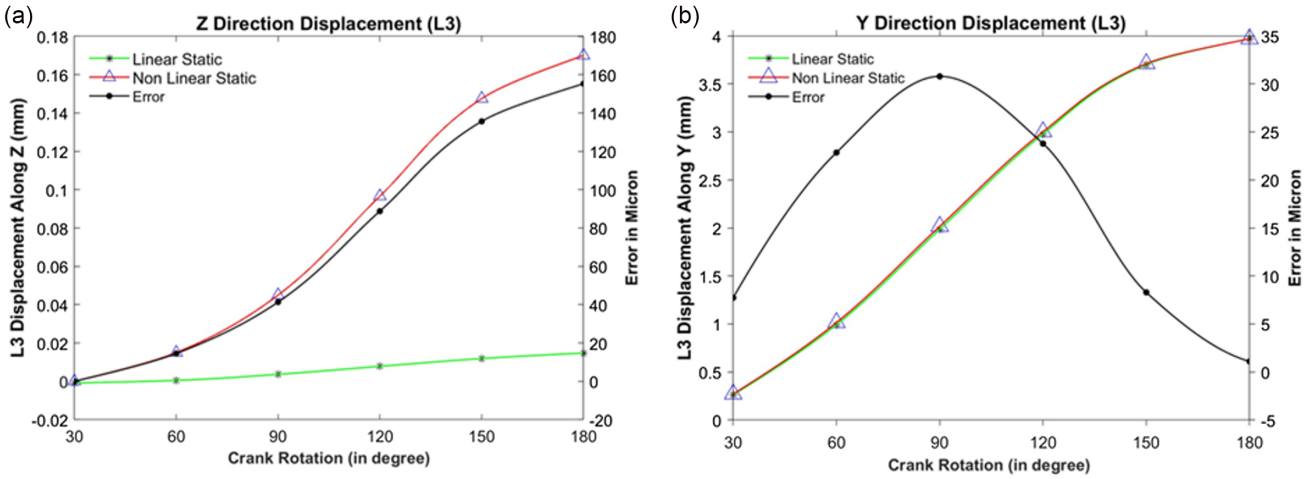

Table 5
Computed tilts in mirror

Mirror	Tilt *X* (arcsec)	Tilt *Y* (arcsec)	Tilt *Z* (arcsec)
*M*1	1.3	2.4	1.5
*M*2	0.8	2.5	0.7
Goal	<±50 arcsec		<±100 arcsec

position which is being further demonstrated in optical test results section.

FE computed results along *Y* direction are mentioned in Table 9 along with measured values for comparison. A maximum displacement of 3.9 mm was attained, compared to an FE value of 3.967 mm. As seen in Figure 13(a), graph plotting these values and the error is displayed. From 0 to 180 degrees, the error keeps

Figure 9
Realized mechanism with different parts

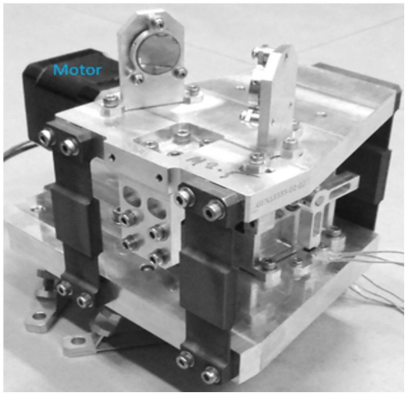

Table 6
Material of different parts of mechanism

Part name	Material
Top plate Bipods Bottom Plate	Aluminium Alloy
Flexural blades Connecting Lever	Titanium Alloy
Crank/eccentric shaft	Stainless steel
Mirrors (*M*1 and *M*2)	Fused Silica
Measured Mass = 1.35 Kg with commercial motor	

Table 7
Specifications of optical elements

Element	Specifications
Lens	Spherical, Diameter 25 mm, effective focal length (EFL) 200 mm
Mirrors	Flat, Diameter 15 mm
Detector	640 × 480 Pixels, 4.8 μ pitch, 8 bit

Figure 10
(a) Designed test setup for displacement measurement and (b) realized test setup

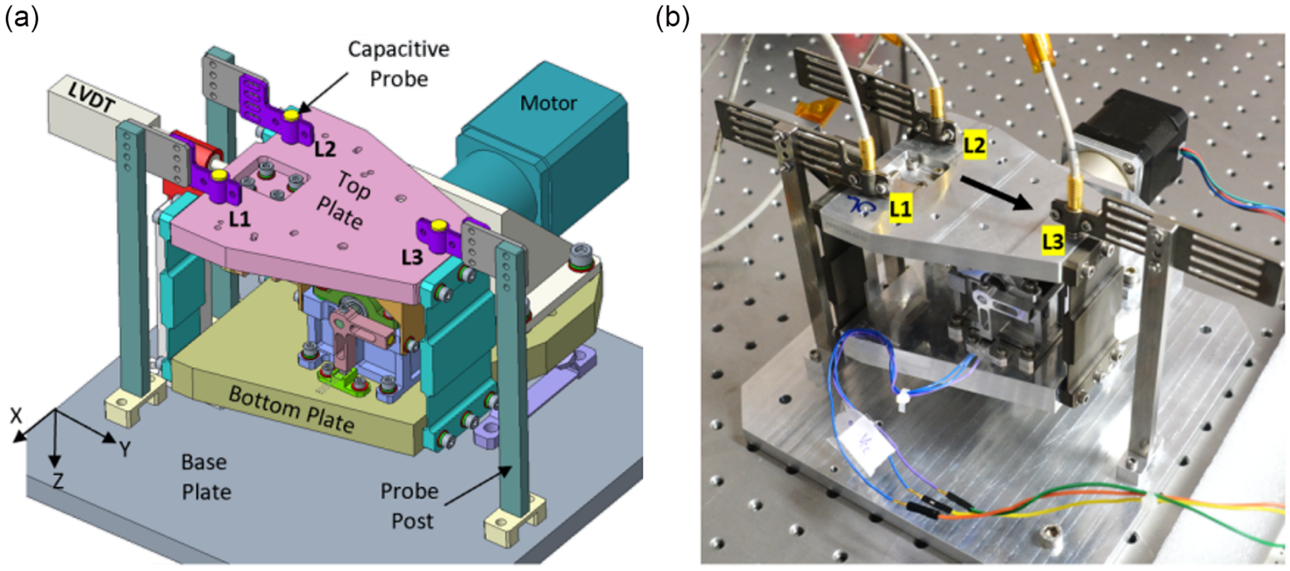

Figure 11
(a) Designed test setup for refocusing measurement and (b) realized test setup

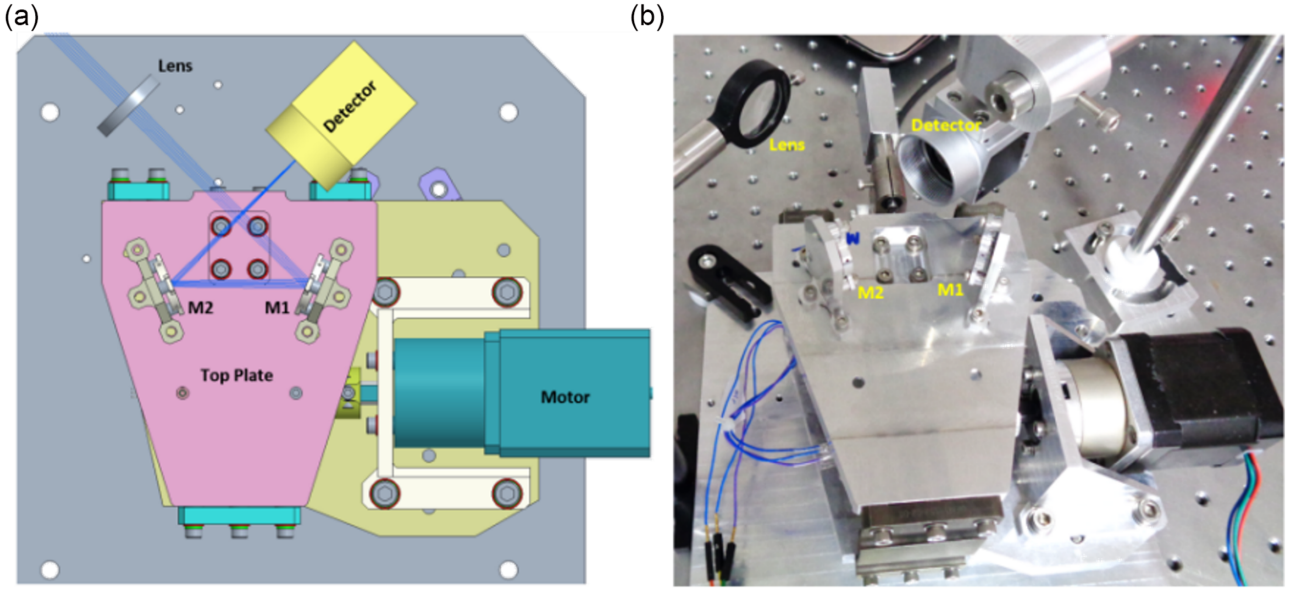

Figure 12
(a) Optical design at focused condition, (b) optical design at defocused condition by 4 mm movement of mirrors along common direction, (c) airy disk diagram at focused condition, (d) airy disk diagram at defocused condition, (e) PSF plot at focus, and (f) PSF plot

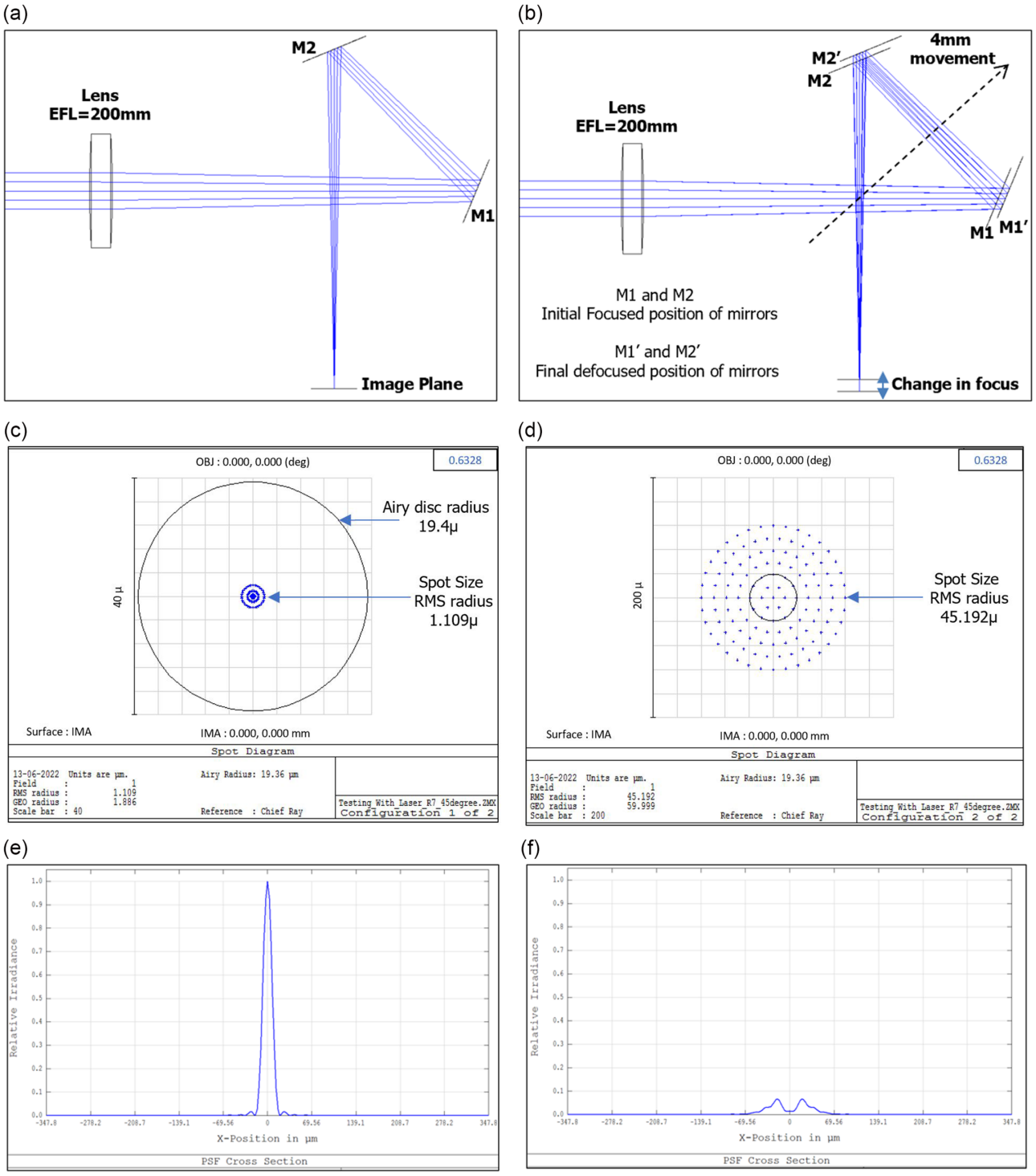

getting bigger. The maximum error is 68 μ at maximum displacement along *Y* direction. The primary cause of this error is achieved eccentricity of fabricated shaft.

FE results along *Z* direction are compared with measured results recorded by capacitive probes. For the three locations that have been identified, *L*1 through *L*3, these results are contrasted in Table 10. At each of the three locations, the eccentricity of the fabricated shaft is the reason for the increasing error between the FE and measured at each step.

Table 8
Measured displacement along *Y* and *Z*

Crank rotation (In degree)	Displacement along *Y* (mm) Measured by LVDT	Displacement along *Z* (mm) measured by capacitive probes		
		Measured *L*1	Measured *L*2	Measured *L*3
30	0.249	−0.002	−0.002	0.000
60	0.984	0.002	0.002	0.013
90	1.971	0.025	0.024	0.042
120	2.945	0.067	0.067	0.092
150	3.648	0.111	0.111	0.142
180	3.899	0.130	0.131	0.162

Table 9
FE and measured displacement along *Y*

Crank rotation (In degree)	Displacement along *Y* (mm)		
	Computed from FE	Measured by LVDT	Error in microns
30	0.271	0.249	22
60	1.014	0.984	30
90	2.015	1.971	44
120	2.999	2.945	54
150	3.708	3.648	60
180	3.967	3.900	68

Figure 13
(a) Comparison graph between FE non-linear vs measured along *Y* and (b) comparison graph between FE linear vs non-linear vs measured along *Z*

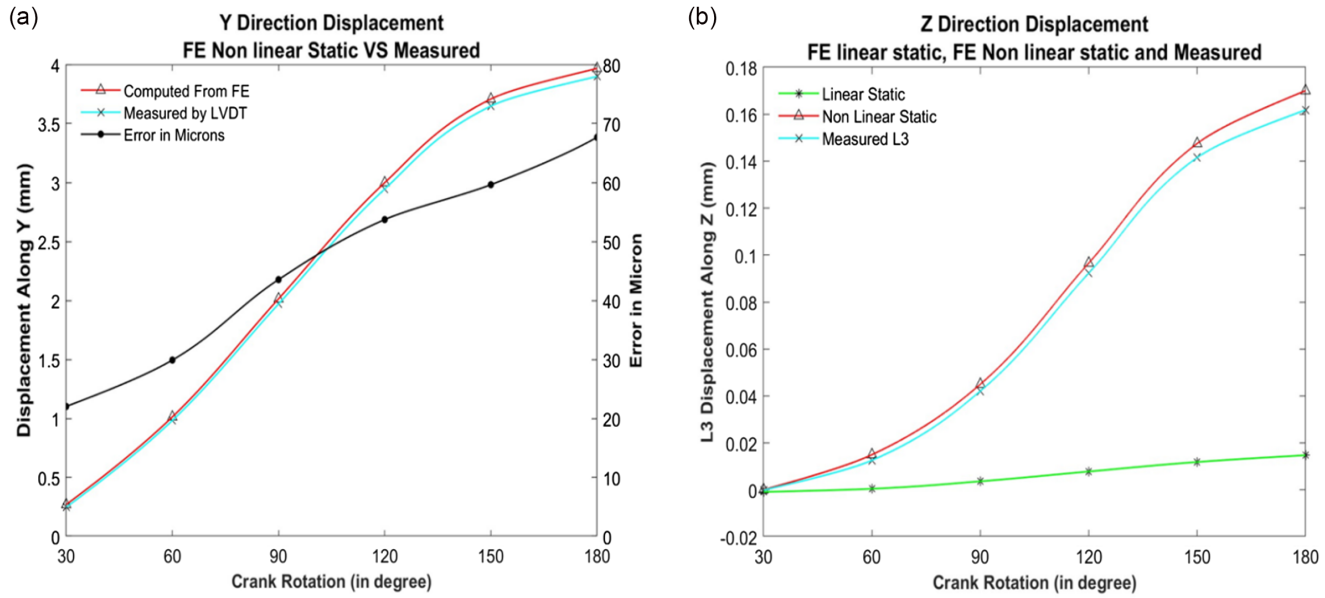

Table 10
FE and measured displacement along *Z*

Crank rotation (In degree)	Displacement along *Z* (mm)					
	FE (*L*1)	Measured *L*1	FE (*L*2)	Measured *L*2	FE (*L*3)	Measured *L*3
30	−0.001	−0.002	0.000	−0.002	0.000	0.000
60	0.006	0.002	0.008	0.002	0.015	0.013
90	0.034	0.025	0.036	0.024	0.045	0.042
120	0.081	0.067	0.084	0.067	0.097	0.092
150	0.128	0.111	0.130	0.111	0.147	0.142
180	0.149	0.130	0.151	0.130	0.170	0.162

A graph of the displacement values at location 3 is provided in Figure 13(b) to enable a thorough investigation of the *Z* direction displacement. It depicts comparison graph of *Z* direction displacement between linear static, non-linear static, and measured. The displacement values computed from linear static analysis are far off from measured values. A good agreement of FE/numerical and experimental results has been found for geometric non-linear static analysis. From Figure 13(b), it is obvious that geometric non-linear static analysis gives more precise prediction of geometric non-linear behavior for additional design optimization. The stiffness/dimensions of flexural blades can be optimized using this technique for minimizing other direction movements and tilts.

5.4. Optical test results

Collimating laser light source of wavelength 633 nm has been used for focusing test. The light travels via a spherical lens first, then hits the *M*1 and *M*2 flat mirrors before focusing at the detector image plane. The detector is initially positioned at best possible optimal focus. For the entire movement of the mechanism, from 0 to 180 degrees, the light intensity counts are recorded at each pixel of the camera. Using the full-width half maxima (FWHM) method, the amount of focus change is calculated. The PSF of the measured intensity counts was used to compute the FWHM. Table 11 shows values of FWHM by design and computed from measured test data at both focused and defocused condition. An image captured by camera when focused is shown in Figure 14(a). Figure 14(b) displays an image that was taken while it was defocused. Figure 14(c) and (d) depict simulated images of galaxy through optical systems under focused and defocused conditions, respectively.

The centroid approach has been utilized to calculate an image's inplane movement. To calculate the centroid, MATLAB was used to process images that were taken during the test at both positions (0 and 180 degrees). As mentioned in Table 12, the centroid is (421.4, 258.5) pixels at focused condition. The calculated centroid of the image is (422.6, 238.1) pixels at the top plate's maximum movement, which is 180 degrees of crank rotation. Figure 15 depicts transition of image from focused to defocused condition and vice versa.

The change in image position along the 640 direction is 20.5 pixels. This resulted mainly due to tilt of top plate about *X*-axis which is computed in Section 5.2 from measured data along *Z* direction. Linear static analysis does not correlate with experiments along *Z* direction. This is why the shift in image position is unknown during the design phase. However, non-linear static analysis correlates well with experiment results along *Z* direction. Using this technique, at design stage the inplane movement of image can be minimized by optimizing design of structural elements. By doing this, the instrument's swath coverage can remain intact.

Table 11
FWHM at focused and defocused condition

Condition	FWHM (Pixels)	
	By design	By test data
Initial 0 degree (Focused)	3.5	3.7
Final 180 degree (Defocused)	12.5	11.6

Figure 14
Test image: (a) at focused condition, (b) at defocused condition, simulated image of galaxy through optical systems, (c) at focused condition, and (d) at defocused condition

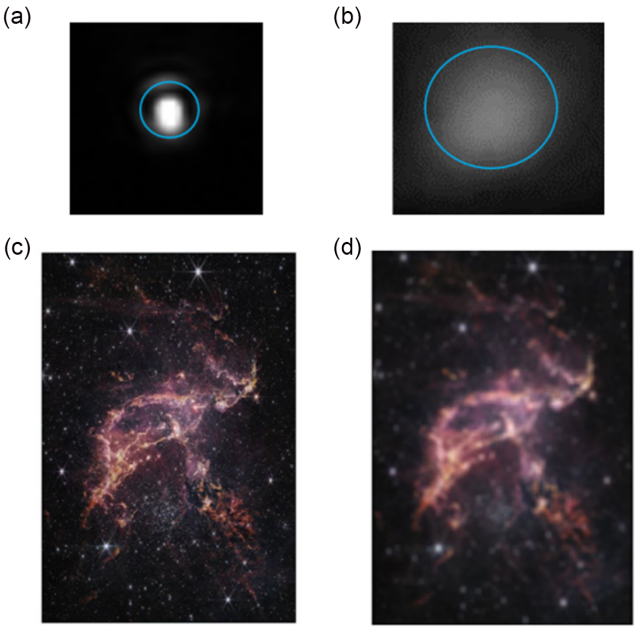

Table 12
Centroid of image

Condition	Centroid (Pixel)	
	Along 640 direction	Along 480 direction (Z direction)
Initial 0 degree (Focused)	421.4	258.5
Final 180 degree (Defocused)	422.6	238.0
Change in image position	1.2	20.5

Figure 15
Inplane shift of image position with zoomed view

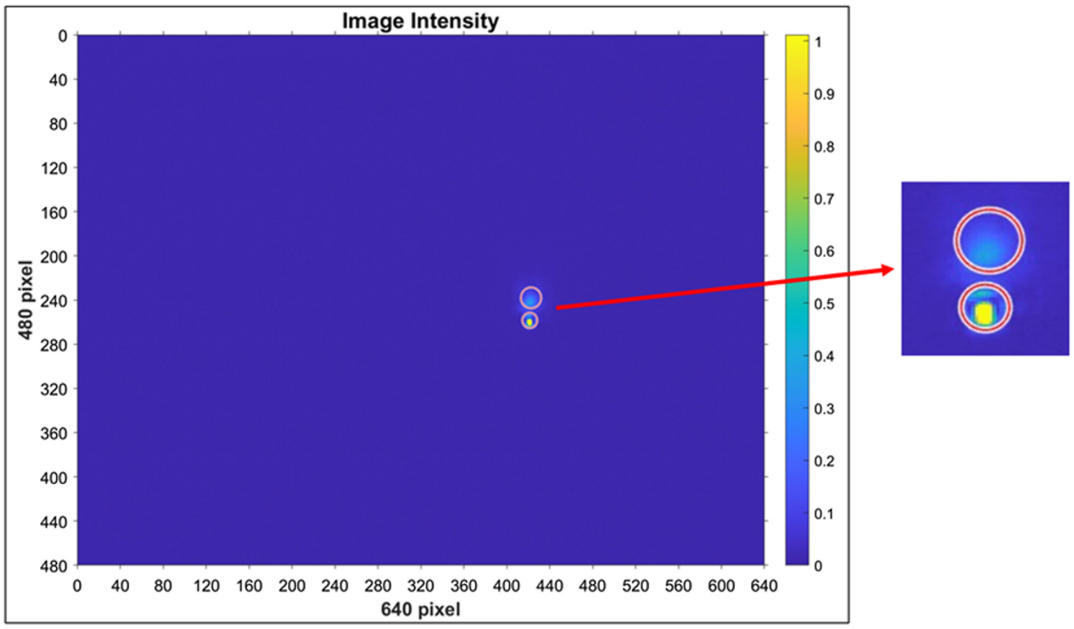

6. Conclusion

The geometric non-linear behavior of large deflection compliant mechanism has been studied by numerically as well as experimentally. A case study that is highly relevant to current deployable optical telescopes is identified for the simulation and validation of geometric non-linearity. The designed refocusing mechanism has 4 mm range from 0 to 180 rotation of eccentric shaft with eccentricity of 2 mm. Linear as well as non-linear static analysis has been performed and outcomes are compared. For the maximum displacement along the *Y* direction, the maximum error is 31 μ, or less than 1%. However, the error is significantly high in the *Z* direction and increases steadily from first to the last step.

In order to validate this behavior, the intended refocusing mechanism has been realized and tested for displacement as well as focus change and image position of optical system. Investigations reveal that the displacement values along the *Z* direction that are calculated using static analysis differ significantly from the measured data. The measured displacement along *Z* direction possesses good agreement with numerically computed by non-linear static analysis. An optical test has validated the shift in focus. At the defocused position, the calculated FWHM is 11.6 pixels compared to the design value of 12.5 pixels. Impact of image position is also demonstrated by optical test. Maximum observed movement of image is 20.5 pixels for complete movement of mechanism from 0 to 180 degree.

This non-linear static analysis technique is helpful in design optimization at initial design stage rather than alternating between linear static analysis and prototype testing through trial and error. It has been applied to the qualification model design optimization process in order to reduce tilts and other direction movements.

Acknowledgement

Authors wish to thank Director, Space Applications Centre, ISRO for approving and providing a rarest opportunity to work on the development of flexure-based mirror refocusing system. We also extend our deepest gratitude to chairman, RF and Optical TDP review committee & its members, who patiently reviewed the work many a time and provided valuable suggestions/ comments, to us without which reaching this goal would be a virtual impossibility.

Ethical Statement

This study does not contain any studies with human or animal subjects performed by any of the authors.

Conflicts of Interest

The authors declare that they have no conflicts of interest to this work.

Data Availability Statement

The data that support the findings of this article cannot be publicly available due to privacy. They can be requested from the corresponding author.

Author Contribution Statement

Yesh Pal: Conceptualization, Methodology, Software, Validation, Formal analysis, Investigation, Resources, Data curation, Writing – original draft, Writing – review & editing, Visualization, Project administration. **Rahul Dev:** Conceptualization, Methodology, Validation, Investigation, Resources, Data curation, Writing – review & editing, Visualization, Supervision, Project administration. **Naimesh R. Patel:** Conceptualization, Methodology, Software, Validation, Formal analysis, Investigation, Resources, Data curation, Writing – review & editing, Visualization, Supervision, Project administration. **Neeraj Mathur:** Conceptualization, Investigation, Resources, Writing – review & editing, Supervision, Project administration. **Shaunak R. Joshi:** Conceptualization, Investigation, Resources, Writing – review &

editing, Supervision, Project administration. **Harshraj Dod:** Software, Validation, Formal analysis, Investigation, Writing – original draft, Writing – review & editing.

References

[1] Laslandes, M., Hugot, E., Ferrari, M., Hourtoule, C., Singer, C., Devilliers, C., ..., & Chazallet, F. (2013). Mirror actively deformed and regulated for applications in space: Design and performance. *Optical Engineering*, *52*(9), 091803. https://doi.org/10.1117/1.OE.52.9.091803

[2] Lightsey, P. A., Atkinson, C. B., Clampin, M. C., & Feinberg, L. D. (2012). James Webb Space Telescope: Large deployable cryogenic telescope in space. *Optical Engineering*, *51*(1), 011003. https://doi.org/10.1117/1.OE.51.1.011003

[3] Han, Y., Zheng, Y., Lin, C., Ji, Z., Xue, H., Li, C., ..., & Gao, Q. (2022). Cryogenic refocusing of an ultrawide FOV long-wave infrared imaging spectrometer in a geostationary orbit. *Remote Sensing*, *14*(22), 5799. https://doi.org/10.3390/rs14225799

[4] Garoli, D., de Marcos, L. V. R., Larruquert, J. I., Corso, A. J., Proietti Zaccaria, R., & Pelizzo, M. G. (2020). Mirrors for space telescopes: Degradation issues. *Applied Sciences*, *10*(21), 7538. https://doi.org/10.3390/app10217538

[5] Li, W., Lv, Q., Zhao, N., Wang, J., Liu, Y., & Zheng, T. (2022). Adaptive thermal refocusing system for a high-resolution space camera. *Applied Optics*, *61*(3), 699–709. https://doi.org/10.1364/AO.443838

[6] Gallardo, P. A., Puddu, R., Harrington, K., Benson, B., Carlstrom, J., Dicker, S. R., ..., & Simon, S. M. (2024). Freeform three-mirror anastigmatic large-aperture telescope and receiver optics for CMB-S4. *Applied Optics*, *63*(2), 310–321. https://doi.org/10.1364/AO.501744

[7] Ling, M., Howell, L. L., Cao, J., & Chen, G. (2020). Kinetostatic and dynamic modeling of flexure-based compliant mechanisms: A survey. *Applied Mechanics Reviews*, *72*(3), 030802. https://doi.org/10.1115/1.4045679

[8] Hao, G., He, X., & Awtar, S. (2019). Design and analytical model of a compact flexure mechanism for translational motion. *Mechanism and Machine Theory*, *142*, 103593. https://doi.org/10.1016/j.mechmachtheory.2019.103593

[9] Abhijit, T., & Prasanna, G. (2022). Design and analysis of ultra-precise large range linear motion platforms using compliant mechanism. *IEEE Access*, *10*, 94321–94336. https://doi.org/10.1109/ACCESS.2022.3201343

[10] Seltmann, S., & Hasse, A. (2023). Topology optimization of compliant mechanisms with distributed compliance (hinge-free compliant mechanisms) by using stiffness and adaptive volume constraints instead of stress constraints. *Mechanism and Machine Theory*, *180*, 105133. https://doi.org/10.1016/j.mechmachtheory.2022.105133

[11] Chen, F., Zhang, Q., Gao, Y., & Dong, W. (2020). A review on the flexure-based displacement amplification mechanisms. *IEEE Access*, *8*, 205919–205937. https://doi.org/10.1109/ACCESS.2020.3037827

[12] Zhu, J., & Hao, G. (2024). Modelling of a general lumped-compliance beam for compliant mechanisms. *International Journal of Mechanical Sciences*, *263*, 108779. https://doi.org/10.1016/j.ijmecsci.2023.108779

[13] Korwar, G. D. (2021). *Kinematic analysis of compliant slider crank mechanism*. Research Square. https://doi.org/10.21203/rs.3.rs-740948/v1

[14] Zhu, B., Zhang, X., Zhang, H., Liang, J., Zang, H., Li, H., & Wang, R. (2020). Design of compliant mechanisms using continuum topology optimization: A review. *Mechanism and Machine Theory*, *143*, 103622. https://doi.org/10.1016/j.mechmachtheory.2019.103622

[15] Kiener, L., Saudan, H., Cosandier, F., Perruchoud, G., Ummel, A., Pejchal, V., ..., & Lichtenberger, M. (2023). Compliant mechanism based on additive manufacturing. *CEAS Space Journal*, *15*(1), 37–53. https://doi.org/10.1007/s12567-021-00394-0

[16] Linß, S., Henning, S., & Zentner, L. (2019). Modeling and design of flexure hinge-based compliant mechanisms. In J. Mizrahi (Ed.), *Kinematics-Analysis and applications* (pp. 41–62). IntechOpen. https://doi.org/10.5772/intechopen.85224

[17] Bilancia, P., & Berselli, G. (2020). Design and testing of a monolithic compliant constant force mechanism. *Smart Materials and Structures*, *29*(4), 044001. https://doi.org/10.1088/1361-665X/ab6884

[18] Tanık, Ç. M., Tanık, E., Yazıcıoğlu, Y., & Parlaktaş, V. (2020). On the analysis and design of a fully compliant large stroke slider-crank (rocker) mechanism. *Mechanical Sciences*, *11*(1), 29–38. https://doi.org/10.5194/ms-11-29-2020

[19] Harfensteller, F., Henning, S., Zentner, L., & Husung, S. (2022). Modeling of corner-filleted flexure hinges under various loads. *Mechanism and Machine Theory*, *175*, 104937. https://doi.org/10.1016/j.mechmachtheory.2022.104937

[20] Mondello, G., di Giampietro, M., & Suetta, E. (2007). The cryogenic refocussing mechanism of NIRSpec. In *12th European Space Mechanisms and Tribology Symposium,* 1–8.

[21] Bahari, A. R., Yunus, M. A., Rani, M. N. A., Ayub, M. A., & Nalisa, A. (2018). Numerical and experimental investigations of nonlinearity behaviour in a slender cantilever beam. In *2018 International Conference on Vibration, Sound and System Dynamics, 217*, 02008. https://doi.org/10.1051/matecconf/201821702008

[22] Bathe, K. J., & Cimento, A. P. (1980). Some practical procedures for the solution of nonlinear finite element equations. *Computer Methods in Applied Mechanics and Engineering*, *22*(1), 59–85. https://doi.org/10.1016/0045-7825(80)90051-1

[23] Gomes, L. L., Barros, F. B., Penna, S. S., & Luiz da Silva Pitangueira, R. (2021). Geometrically nonlinear analysis by the generalized finite element method. *Engineering Computations*, *38*(1), 266–288. https://doi.org/10.1108/EC-10-2019-0478

[24] Henning, S., Linß, S., Gräser, P., Theska, R., & Zentner, L. (2021). Non-linear analytical modeling of planar compliant mechanisms. *Mechanism and Machine Theory*, *155*, 104067. https://doi.org/10.1016/j.mechmachtheory.2020.104067

[25] Bathe, K. J. (1996). *Finite element procedures*. USA: Prentice Hall.

[26] Micro-Epsilon. (n.d.). *Capacitive sensors for displacement, distance and position*. https://www.micro-epsilon.com/distance-sensors/capacitive-sensors

How to Cite: Pal, Y., Dev, R., Patel, N. R., Mathur, N., Joshi, S. R., & Dod, H. (2026). Structural Analysis Technique and Its Validation for Large Range Mirror Refocusing System for Spaceborne Deployable Telescopes. *Journal of Optics and Photonics Research*, *3*(2), 109–121. https://doi.org/10.47852/bonviewJOPR42022660